Applied Catalysis B: Environmental 220 (2018) 542–552

Contents lists available at ScienceDirect

Applied Catalysis B: Environmental

journal homepage: www.elsevier.com/locate/apcatb

Preparation of 2D/2D g-C_3N_4 nanosheet@$ZnIn_2S_4$ nanoleaf heterojunctions with well-designed high-speed charge transfer nanochannels towards high-efficiency photocatalytic hydrogen evolution

Bo Lin[a], He Li[a], Hua An[a], Wenbin Hao[a], JinJia Wei[a], Yanzhu Dai[b], Chuansheng Ma[b], Guidong Yang[a,*]

[a] XJTU-Oxford International Joint Laboratory for Catalysis, School of Chemical Engineering and Technology, Xi'an Jiaotong University, Xi'an 710049, China
[b] Electronic Materials Research Laboratory, Key Laboratory of the Ministry of Education, Center for Dielectric Research, Xi'an Jiaotong University, Xi'an 710049, China

ARTICLE INFO

Keywords:
2D/2D heterojunction
g-C_3N_4 nanosheet
$ZnIn_2S_4$ nanoleaf
High-speed charge transfer nanochannel
Photocatalytic hydrogen evolution

ABSTRACT

In this work, we design and construct a novel 2D/2D g-C_3N_4 nanosheet@$ZnIn_2S_4$ nanoleaf via a simple one-step surfactant-assisted solvothermal method for photocatalytic H_2 generation. Its unusual 2D/2D heterojunction structure provides far more contact areas and much faster charge transport rate than the 2D/0D heterojunction structure of g-C_3N_4 nanosheet@$ZnIn_2S_4$ microsphere. More importantly, this unique 2D/2D heterojunction leads the g-C_3N_4 nanosheet@$ZnIn_2S_4$ nanoleaf composite to generate numerous intimate high-speed charge transfer nanochannels in the interfacial junctions, and which could considerably enhance the photogenerated charge separation and migration efficiency, thus yielding a remarkable visible-light-driven H_2 evolution rate without the additive Pt cocatalyst (HER = 2.78 mmol h^{-1} g^{-1}), nearly 69.5, 15.4, 8.2 and 1.9 times higher than that of pure g-C_3N_4 nanosheet, pure $ZnIn_2S_4$ microsphere, 2D/0D g-C_3N_4 nanosheet@$ZnIn_2S_4$ microsphere and pure $ZnIn_2S_4$ nanoleaf, respectively. Additionally, the 2D/2D g-C_3N_4 nanosheet@$ZnIn_2S_4$ nanoleaf exhibits an outstanding stability and recyclability, manifesting a promising potential application in sustainable energy conversion. This work would provide a platform for the design and synthesis of binary heterojunction composite system with highly-efficient charge separation and transfer.

1. Introduction

The high-efficiency utilization of solar energy is a desirable and scalable strategy to handle the crises of ever growing global energy demand and severe environmental concerns. The semiconductor photocatalysis technology is precisely the key to advance the sunlight exploitation into feasible industrial applications, such as energy conversion [1,2], environmental protection [3,4], and organic synthesis [5,6]. Nevertheless, the considerably high recombination rate of photoexcited electron-hole pairs for single-component photocatalysts is the major obstacle to achieve a high quantum efficiency and photocatalytic activity, thus limiting the practical application of photocatalysis technology, just like single pristine bulk graphitic carbon nitride (g-C_3N_4), which although has gained considerable attention due to its attractive electronic and optical properties, facilely tunable electronic structure, remarkable chemical and thermal stability, low economic cost and environmental friendliness [7–9], the g-C_3N_4 still shows quite low photocatalytic activity with quantum efficiency of approximately 0.1% under visible-light irradiation owing to its highly photogenerated charge recombination rate [10,11]. Therefore, significant efforts have been made to design and construct the multicomponent heterostructured photocatalysts which could effectively accelerate the separation and migration of photogenerated charges, and this design strategy has been shown huge advantages for the enhancement of visible-light photocatalytic activity of g-C_3N_4-based heterostructured composite.

Recently, as a new and important member in the community of ternary chalcogenide (simplified as AB_2X_4, A = Zn, Ca, Cu, Cd; B = Al, Ga, In; X = S, Se, Te), $ZnIn_2S_4$ with a typical layered structure has triggered keen interest in photocatalysis due to its excellent electrical and optical properties, strong visible-light harvesting ability and remarkable chemical stability [12–14]. More importantly, as previously reported [10,12,15], $ZnIn_2S_4$ has a matched band gap structure with g-C_3N_4, which makes it possible to construct the binary heterojunction system of g-C_3N_4@$ZnIn_2S_4$ to improve the charge separation and migration efficiency for g-C_3N_4. In the recent work, Liu and Jin *et al.* [12]

* Corresponding author.
E-mail address: guidongyang@xjtu.edu.cn (G. Yang).

http://dx.doi.org/10.1016/j.apcatb.2017.08.071
Received 16 May 2017; Received in revised form 12 July 2017; Accepted 20 August 2017
Available online 24 August 2017

have reported the synthesis of $ZnIn_2S_4$@g-C_3N_4 nanocomposites using the hydrothermal method, which exhibits high photocatalytic hydrogen evolution. Liu and Chen *et al.* [15] have also fabricated g-C_3N_4 nanosheet@$ZnIn_2S_4$ nanoparticles with an improved photocatalytic activity using a hydrothermal strategy. However, these above conventionally prepared g-C_3N_4@$ZnIn_2S_4$ binary composites present a typical 2D/0D type (face-to-point) heterojunction, and the 2D/0D heterojunction owns the micron-sized bulk aggregate structure and very small contacted interface between g-C_3N_4 nanosheet and $ZnIn_2S_4$ agglomerate, thus a severe traffic congestion of charges can be easily happened in the contacted interface. Besides, the photogenerated charges on the inside of the $ZnIn_2S_4$ agglomerates have to transfer along the longer route to the $ZnIn_2S_4$ surfaces in the photocatalytic reaction. These above charge transfer processes would lead to the poor charge separation and migration efficiency as well as low photocatalytic activity for 2D/0D $ZnIn_2S_4$@g-C_3N_4 composite. Hence, the design of effective heterojunction with intimate interface contact between g-C_3N_4 and $ZnIn_2S_4$ is considered to be a promising protocol to significantly accelerate the charge separation and migration in the binary heterojunction system of g-C_3N_4@$ZnIn_2S_4$.

According to the aforementioned motivation, the 2D/2D heterojunction is precisely the desired heterojunction that we earnestly seek. From the viewpoint of binary two-dimensional g-C_3N_4-based heterojunction microstructures, the 2D/2D type g-C_3N_4@$ZnIn_2S_4$ heterojunction owns many unique advantages by contrast with 2D/0D type one [16,17]: Firstly, the 2D/2D face-to-face heterojunction formed between g-C_3N_4 nanosheet and $ZnIn_2S_4$ nanosheet has much more contact areas than the 2D/0D face-to-point g-C_3N_4@$ZnIn_2S_4$ composite. Secondly, the 2D/2D type g-C_3N_4@$ZnIn_2S_4$ heterojunction shortens the migration distance and time of photoinduced charges. Therefore, the construction of 2D/2D type heterojunction can produce a lot of unique high-speed charge transfer nanochannels in g-C_3N_4@$ZnIn_2S_4$ composite, which mean that the photoinduced charges transfer along the expected migration route (from g-C_3N_4 nanosheet to the intimate heterojunction interface then to $ZnIn_2S_4$ nanosheet), similarly to the freeways in real life, thus contributing to the fairly high charge separation and transfer efficiency as well as outstanding photocatalytic activity. However, thus far, no report has been available on the construction of 2D/2D g-C_3N_4 nanosheet@$ZnIn_2S_4$ nanosheet photocatalyst.

Herein, we first design and construct a novel 2D/2D g-C_3N_4 nanosheet@$ZnIn_2S_4$ nanoleaf (a nano-sized $ZnIn_2S_4$ sheet similarly to the leaf in nature) with the unique high-speed charge transfer nanochannels achieved by in-situ growing unique $ZnIn_2S_4$ nanoleaves on the surfaces of g-C_3N_4 nanosheets via a simple one-step surfactant-assisted solvothermal method. The resultant 2D/2D g-C_3N_4 nanosheet@$ZnIn_2S_4$ nanoleaf exhibits a remarkable hydrogen evolution activity without the additive Pt cocatalyst, far exceeding the 2D/0D g-C_3N_4 nanosheet@$ZnIn_2S_4$ microsphere. Various characterization methods, such as XRD, SEM, TEM, DRS, PL and transient fluorescence decay spectra, are explored to shed light on the intrinsic link between the 2D/2D geometry structure and significantly enhanced photocatalytic activity for the resultant g-C_3N_4 nanosheet@$ZnIn_2S_4$ nanoleaf heterojunction.

2. Experimental

2.1. Material synthesis

All reagents for synthesis and analysis were analytical grade and used without further purification.

2.1.1. Synthesis of bulk g-C_3N_4

10 g of melamine was directly calcined at 550 °C for 4 h in air with a heating rate of 2.3 °C·min^{-1}, the resultant canary powder was collected as a reference and denoted as BCN.

2.1.2. Synthesis of g-C_3N_4 nanosheet

3 g of above bulk g-C_3N_4 was exposed to air and calcined at 520 °C for 5 h, the resultant white powder was collected for the further use and denoted as CNNs.

2.1.3. Synthesis of pure $ZnIn_2S_4$ nanoleaf

0.030 g of $Zn(NO_3)_2 \cdot 6H_2O$ (0.1 mmol), 0.076 g of $In(NO_3)_3 \cdot 4.5H_2O$ (0.2 mmol) and a certain amount of trisodium citrate dihydrate were dissolved in 30 mL of deionized water, and vigorously stirred at room temperature for 0.5 h. Then 0.060 g of thioacetamide (TAA, 0.8 mmol) was ultrasonically dissolved in the above solution and vigorously stirred at same temperature for 0.5 h. Next, the above mixture solution was transferred to a 100 mL Teflon-lined stainless steel autoclave and heated at 160 °C for 1 h. After cooling down to room temperature, the sample was collected by the centrifugation, washed several times using deionized water and ethanol, and dried in a drying oven at 60 °C for 24 h. The resultant product was denoted as PZN. As a reference, the pure $ZnIn_2S_4$ microsphere was synthesized under the similar conditions, and the only difference is the lack of trisodium citrate dihydrate. The resultant pure $ZnIn_2S_4$ microsphere was denoted as PZM.

2.1.4. Synthesis of 2D/2D g-C_3N_4 nanosheet@$ZnIn_2S_4$ nanoleaf

The 2D/2D g-C_3N_4 nanosheet@$ZnIn_2S_4$ nanoleaf was synthesized by a simple surfactant-assisted solvothermal method. In detail, 0.030 g of $Zn(NO_3)_2 \cdot 6H_2O$ (0.1 mmol), 0.076 g of $In(NO_3)_3 \cdot 4.5H_2O$ (0.2 mmol) and a certain amount of trisodium citrate dihydrate were dissolved in 30 mL of deionized water, and vigorously stirred at room temperature for 0.5 h. Then 0.020 g of g-C_3N_4 nanosheet was ultrasonically dispersed in the above solution and vigorously stirred at same temperature for 3 h. Next, 0.060 g of thioacetamide (TAA, 0.8 mmol) was ultrasonically dissolved in the above solution and vigorously stirred at same temperature for 0.5 h. Finally, the above mixture solution was transferred to a 100 mL teflon-lined stainless steel autoclave and heated to 160 °C and kept for 1 h. After cooling down to room temperature, the sample was collected by the centrifugation, washed several times using deionized water and ethanol, and dried in drying oven at 60 °C for 24 h. The resultant product was denoted as GN@ZN. Furthermore, the 2D/0D g-C_3N_4 nanosheet@$ZnIn_2S_4$ microsphere was synthesized as a reference. The preparation process of 2D/0D g-C_3N_4 nanosheet@$ZnIn_2S_4$ microsphere is similar to that of GN@ZN, and the only difference is the lack of trisodium citrate dihydrate. The resultant 2D/0D g-C_3N_4 nanosheet@$ZnIn_2S_4$ microsphere was denoted as GN@ZM. Additionally, a mechanically mixed g-C_3N_4 nanosheet@$ZnIn_2S_4$ nanoleaf (MMGZ) sample was also obtained by finely grinding 0.2 g of g-C_3N_4 nanosheet and 0.4 g of pure $ZnIn_2S_4$ nanoleaf.

2.2. Characterization

The as-prepared products were characterized by a variety of techniques. The crystal structure of products was analyzed with the help of a powder X-ray diffraction (Lab X XRD-6100, SHIMADZU). The morphologies of the resultant samples were observed by a field emission scanning electron microscope (JSM-6700F, JEOL) and a transmission electron microscopy (JEM-2100, JEOL). The elementary composition of samples was analyzed by the energy dispersive X-ray spectroscopy (EDX) and elemental mapping. The Brunauer-Emmett-Teller (BET) specific surface areas were recorded on an automatic BET analyzer (Autosorb-iQ-TPX, Auantachrome), and the products were degassed at 160 °C for 6 h before the N_2 adsorption measurements. Steady photoluminescence (PL) emission spectra and transient fluorescence decay spectra were tested by a luminescence spectrophotometer (QM-400, PTI) with 340 nm excitation wavelength. Ultraviolet-visible (UV-vis) diffuse reflectance spectra (DRS) were obtained using a UV–vis spectrophotometer (UV-2600, SHIMADZU). Additionally, the valence band (E_{VB}) and conduction band (E_{CB}) edge

potentials of samples can be determined by the following two formulas:

$$E_{VB} = X\text{-}E_e + 0.5 \times E_g \quad (1)$$

$$E_{CB} = E_{VB} - E_g \quad (2)$$

Where E_e represents the free electron energy on the hydrogen scale (4.5 eV), and X represents the absolute electronegativity of semiconductor materials. The X values for g-C_3N_4 and $ZnIn_2S_4$ are 4.73 eV and 4.86 eV, respectively [4,12].

2.3. Photocatalytic activity measurement

The photocatalytic hydrogen production was conducted in an outer Pyrex reactor (100 mL). 0.05 g of powder photocatalyst was suspended into an aqueous solution (50 mL) containing 10 mL of triethanolamine (sacrificial electron donor). Prior to the reaction, the reaction solution was deaerated by the bubbled treatment with high purity nitrogen to remove air completely. Then the reaction was carried out under the illumination of a 300 W Xenon lamp (HSX-F300, NbeT, Beijing) equipped with a 420 nm cutoff filter. The evolved gases were detected by a gas chromatograph (SP-2100A, Beifen-Ruili) equipped with a 5 Å molecular sieve and a TCD detector.

The apparent quantum yield (AQY) for the obtained samples was tested under the same reaction conditions, the only difference is that a 420 nm band-pass filter is used to obtain the monochromatic light (λ = 420 nm), and the average irradiation intensity received by the reactor is 52.8 mW cm^{-2}. The AQY was evaluated by the following equation:

$$AQY(\%) = \frac{2 \times \text{number of evolved hydrogen molecules}}{\text{number of incident photons}} \quad (3)$$

2.4. Photoelectrochemical measurement

The photocurrent response and electrochemical impedance spectroscopy of the samples were tested by a CHI 660D type electrochemical station (Chenhua, China) and a PMC-1000/DC type one (AMETEK), respectively. The two kinds of measurements are in the same three-electrode system. In this system, the Na_2SO_4 aqueous solution (1 M) was used as the electrolyte. The Ag/AgCl electrode and platinum wire were chosen as the reference electrode and the counter electrode, respectively. The glassy carbon electrodes containing the as-prepared products were served as the working electrodes.

3. Results and discussion

The overall formation procedure of 2D/2D g-C_3N_4 nanosheet@$ZnIn_2S_4$ nanoleaf is presented in Fig. 1. Firstly, the initial bulk g-C_3N_4 (BCN) was fabricated by the thermal-induced self-condensation of melamine heating at 550 °C for 4 h in air. Thereafter, the BCN was exfoliated and transformed into g-C_3N_4 nanosheet (CNNs) via a thermal oxidation process calcining at 520 °C for 5 h in air. When the CNNs was dispersed and stirred in the aqueous solution containing Zn$(NO_3)_2 \cdot 6H_2O$, In$(NO_3)_3 \cdot 4.5H_2O$ and trisodium citrate dihydrate, the cations of Zn^{2+} and In^{3+} readily loaded on the surfaces of negatively charged CNNs through electrostatic attraction effect [10]. After that, along with the addition of thioacetamide, the generated S^{2-} reacted with absorbed Zn^{2+} and In^{3+} to obtain numerous $ZnIn_2S_4$ nanoparticles on the CNNs flat. It is noted that the generated $ZnIn_2S_4$ nanoparticles would be covered by the trisodium citrate dihydrate molecules, which effectively restrain the growth of $ZnIn_2S_4$ and make it slowly change into nanoleafy structure with an average length of 55 nm and an average width of 10 nm under the solvothermal condition. Ultimately, a large number of $ZnIn_2S_4$ nanoleaves uniformly distribute on the CNNs flat in the unique face-to-face way to obtain 2D/2D g-C_3N_4@$ZnIn_2S_4$ binary heterojunction system.

Fig. 2 exhibits the typical X-ray diffraction (XRD) patterns of the obtained products. As shown in Fig. 2a, two evident characteristic peaks could be clearly observed in the curves of BCN and CNNs. The minor diffraction peak at 12.9° corresponds to the (100) crystal plane of g-C_3N_4 derived from the repetitive in-plane structural packing motif of tri-s-triazine units [18]. In regard to the initial BCN sample, the prominent and sharp diffraction peak at 27.4° can be assigned to the interlayer-stacking (002) reflection of melon networks [19]. It is noteworthy that the (002) reflection peak in the curve of CNNs displays the relatively weak intensity and a tiny shift from 27.4° to 27.7°, this shift is due to the reduced interplane distance after thermal oxidation exfoliation treatment [19]. With respect to the samples of pure $ZnIn_2S_4$ microsphere and pure $ZnIn_2S_4$ nanoleaf, as displayed in Fig. 2b, all XRD diffraction peaks belong to the hexagonal crystal structure of $ZnIn_2S_4$ (a = b = 3.85 Å, c = 24.68 Å), which well conforms to the JCPDS data (ICDD-JCPDS card no. 72-0773) [13,20,21]. For the products of 2D/0D GN@ZM and 2D/2D GN@ZN, a strong diffraction peak at around 27.9° appeared in both of the curves can be attributed to the overlap of the (002) reflection peak of g-C_3N_4 nanosheet (27.7°) and the (102) reflection peak of hexagonal $ZnIn_2S_4$ (28.2°). Additionally, all other diffraction peaks in the two composite samples are corresponded to the crystal planes of hexagonal $ZnIn_2S_4$, indicating the successful formation of g-C_3N_4@$ZnIn_2S_4$ binary heterojunction composite.

The morphologies of the resultant products are measured by the scanning electron microscopy (SEM, Fig. 3) and transmission electron microscopy (TEM, Fig. 4). Figs. 3a and 4a show the typical micron-sized bulk morphology for BCN. It can be seen that the bulk g-C_3N_4 has been exfoliated into a thinner g-C_3N_4 nanosheet after thermal oxidation exfoliation (Figs. 3b and 4b), and the formation of g-C_3N_4 nanosheet can effectively shorten the vertical movement distance of photoinduced charges and thus restrain the charge recombination in the inside of g-C_3N_4. In regard to PZM, it can be clearly found that several $ZnIn_2S_4$ microspheres aggregate to form irregular agglomerates (Figs. 3c and 4c). However, with the help of trisodium citrate dihydrate, numerous uniformly dispersed $ZnIn_2S_4$ nanosheets similarly to the leaves in nature are shown in SEM and TEM images of PZN (Figs. 3d and 4d), and the individual $ZnIn_2S_4$ nanoleaf has an average length of 55 nm and an average width of 10 nm (see the inset of Fig. 4d). The novel nano-sized leafy morphology is beneficial for the charge separation, significantly promoting the enhancement of photocatalytic activity. In Figs. 3e and 4e, many irregular $ZnIn_2S_4$ agglomerates, like microsphere structure, randomly disperse on the flat of CNNs in the face-to-point way to obtain 2D/0D g-C_3N_4@$ZnIn_2S_4$ binary heterojunction composite, this 2D/0D type heterojunction has an extremely limited contact area, and tends to cause a serious traffic congestion when the photogenerated charges transfer through the contact area, resulting in a slow charge transport

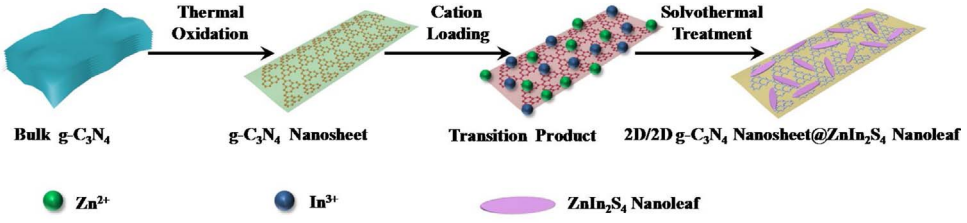

Fig. 1. Schematic sketch of formation procedure of 2D/2D g-C_3N_4 nanosheet@$ZnIn_2S_4$ nanoleaf.

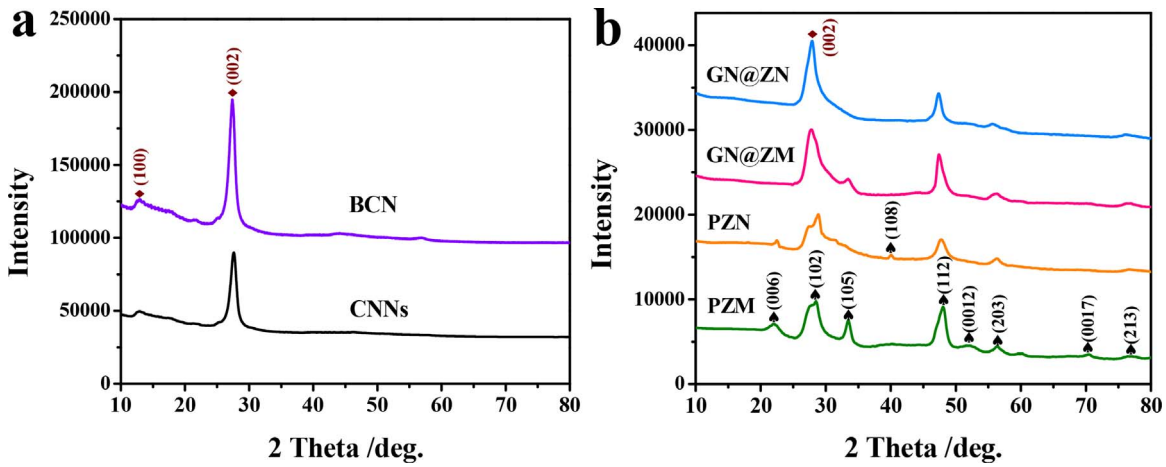

Fig. 2. (a) X-ray diffraction patterns of BCN and CNNs. (b) X-ray diffraction patterns of PZM, PZN, GN@ZM and GN@ZN.

rate. Differing from 2D/0D GN@ZM, the sample of 2D/2D GN@ZN shows an optimal g-C_3N_4@$ZnIn_2S_4$ heterojunction structure (Figs. 3f and 4f): Massive well-dispersed nanoscale $ZnIn_2S_4$ nanoleaves uniformly grow on the surfaces of g-C_3N_4 nanosheet flat. The magnification TEM (Fig. 4g, h) further manifests the $ZnIn_2S_4$ nanoleaves sufficiently contact with g-C_3N_4 nanosheet in the face-to-face way and thus form vast effective heterojunction interfaces. This unique spatial arrangement of g-C_3N_4 and $ZnIn_2S_4$ in 2D/2D GN@ZN could create abundant high-speed charge transfer nanochannels, greatly improving charge separation and migration efficiency. The HR-TEM image of 2D/2D GN@ZN (Fig. 4i) clearly confirms the presence of intimate 2D/2D heterojunction interface, where the lattice-fringe spacing of 0.321 nm is indexed to the (102) reflection plane of hexagonal $ZnIn_2S_4$, and this (102) reflection plane is attached closely to the amorphous area of g-C_3N_4 to form the 2D/2D heterojunction. Additionally, to further investigate the compositions and element distributions of 2D/2D GN@ZN, the energy-dispersive X-ray (EDX) elemental mapping tests are performed. As shown in Fig. 5a–f, the elemental mappings clearly reveal the uniform spatial distribution of rich elements, including carbon (C), nitrogen (N), zinc (Zn), indium (In) and sulfur (S), indicating that $ZnIn_2S_4$ nanoleaves uniformly distribute on the surfaces of g-C_3N_4 nanosheet flat, strongly supporting the SEM and TEM observations. The above-mentioned elements in 2D/2D GN@ZN are also confirmed by EDX measurement (Fig. 5g, h).

Time-dependent photoinduced H_2 evolution for different photocatalysts has been carried out in an aqueous solution containing triethanolamine (sacrificial electron donor) without the additive Pt cocatalyst under visible-light irradiation ($\lambda \geq 420$ nm). As illustrated in Fig. 6a, the pristine g-C_3N_4 displays negligible hydrogen-evolution rate (HER), and after the thermal exfoliation treatment, the g-C_3N_4 nanosheet shows an enhanced HER value (0.04 mmol h^{-1} g^{-1}), manifesting the structure-induced merits of g-C_3N_4 nanosheet. Moreover, the PZM sample exhibits moderate HER of 0.18 mmol h^{-1} g^{-1}. Interestingly, the PZN sample shows dramatically increased HER (1.46 mmol h^{-1} g^{-1}), nearly 8.1 times higher than that of PZM, strongly supporting the advantages of size control technology. When it comes to the g-C_3N_4@$ZnIn_2S_4$ binary heterojunction system, its structural advantages are directly reflected on the photocatalytic activity:

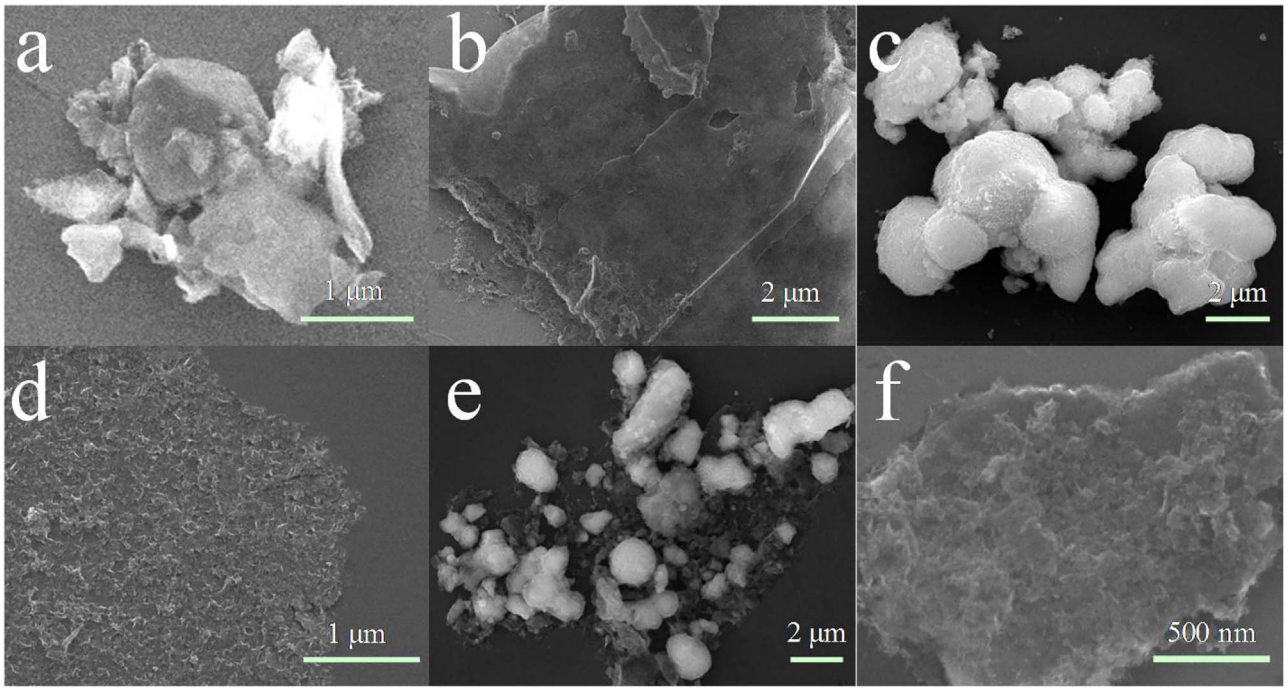

Fig. 3. SEM images of (a) BCN, (b) CNNs, (c) PZM, (d) PZN, (e) GN@ZM and (f) GN@ZN.

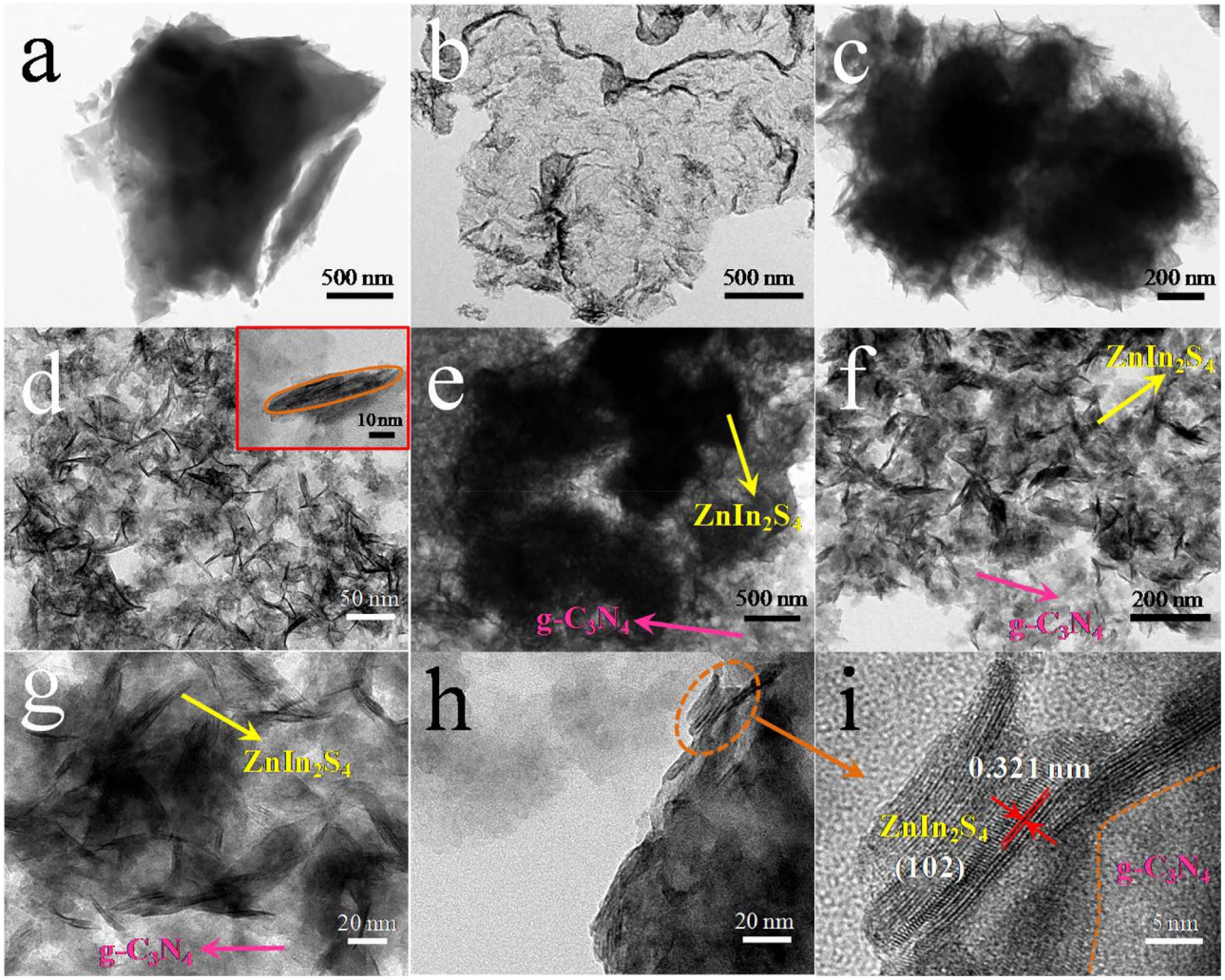

Fig. 4. TEM images of (a) BCN, (b) CNNs, (c) PZM, (d) PZN, (e) GN@ZM and (f) GN@ZN. Inset in (d): The magnification TEM image of individual $ZnIn_2S_4$ nanoleaf. The magnification TEM (g, h) of GN@ZN. HR-TEM image (i) of GN@ZN.

The 2D/0D GN@ZM has a HER of 0.34 mmol h^{-1} g^{-1}, which is 1.89 times higher than that of PZM. Incredibly, the 2D/2D GN@ZN exhibits remarkable photocatalytic activity (2.78 mmol h^{-1} g^{-1}), and this value is nearly 69.5, 15.4, 8.2 and 1.9 times higher than that of CNNs, PZM, 2D/0D GN@ZM and PZN, respectively. More importantly, the HER of 2D/2D GN@ZN also far exceeds that of the majority of modified g-C_3N_4 in previous reports, even including numerous Pt-deposited photocatalysts (Fig. 6b) [7,12,22–32], indicative of the great advantages of the special 2D/2D heterojunction with high-speed charge transfer nanochannels. For comparison, a mechanically mixed g-C_3N_4 nanosheet and $ZnIn_2S_4$ nanoleaf sample was also synthesized, and the sample shows an extremely poor HER (0.02 mmol h^{-1} g^{-1}), again demonstrating the importance of the 2D/2D heterojunction for the photocatalytic H_2 evolution activity. To intuitively understand the significantly enhanced photocatalytic activity of 2D@2D heterojunction, the AQY of all the products has been measured under the monochromatic light irradiation (λ = 420 nm). Both BCN and MMGZ samples show the negligible AQY value, while CNNs displays an extremely low AQY value of 0.01%. The PZN sample exhibits an AQY value of 3.80%, which is much higher than that of PZM sample (0.55%) due to its special leafy nanostructure. Furthermore, the 2D/2D GN@ZN owns the incredible AQY value of 7.05%, far outperforming the 2D/0D GN@ZM (1.01%). The results show that the construction of 2D/2D heterostructure is greatly beneficial for the enhancement of photocatalytic activity of g-C_3N_4 sample.

The stability and recyclability for the visible-light-driven photocatalytic hydrogen evolution over 2D/2D GN@ZN have been investigated under the same conditions. As shown in Fig. 6c, the resultant 2D/2D GN@ZN still maintains high photocatalytic hydrogen evolution activity after four photoreactions. Moreover, the TEM images in Fig. 7a show that the cyclic GN@ZN sample remains an intact morphology of the typical 2D/2D face-to-face structure after four photoreactions, similarly to the fresh 2D/2D GN@ZN sample (shown in Fig. 4f, g). Additionally, there is no obvious difference in the XRD patterns in both 2D/2D GN@ZN products before and after four photoreactions (Fig. 7b). These all prove that the novel 2D/2D g-C_3N_4 nanosheet@$ZnIn_2S_4$ nanoleaf has an outstanding stability and recyclability, manifesting a promising potential application in sustainable energy conversion.

As shown in Fig. 6a, b, the construction of 2D/2D g-C_3N_4 nanosheet@$ZnIn_2S_4$ nanoleaf heterostructure contributes to the remarkable activity for photocatalytic hydrogen evolution without the additive Pt cocatalyst, this would offer a new idea for the design and preparation of binary heterojunction composite system with the excellently catalytic performances. In order to better understand the effects of 2D/2D geometry structure on the above-mentioned outstanding photocatalytic activity for 2D/2D GN@ZN, it is necessary to discuss the origin of the significantly improved photocatalytic activity. As we know, the following factors, including optical absorption capacity, active surface area, photoinduced charge separation and migration efficiency, are three key scientific issues to influence the photocatalytic activity.

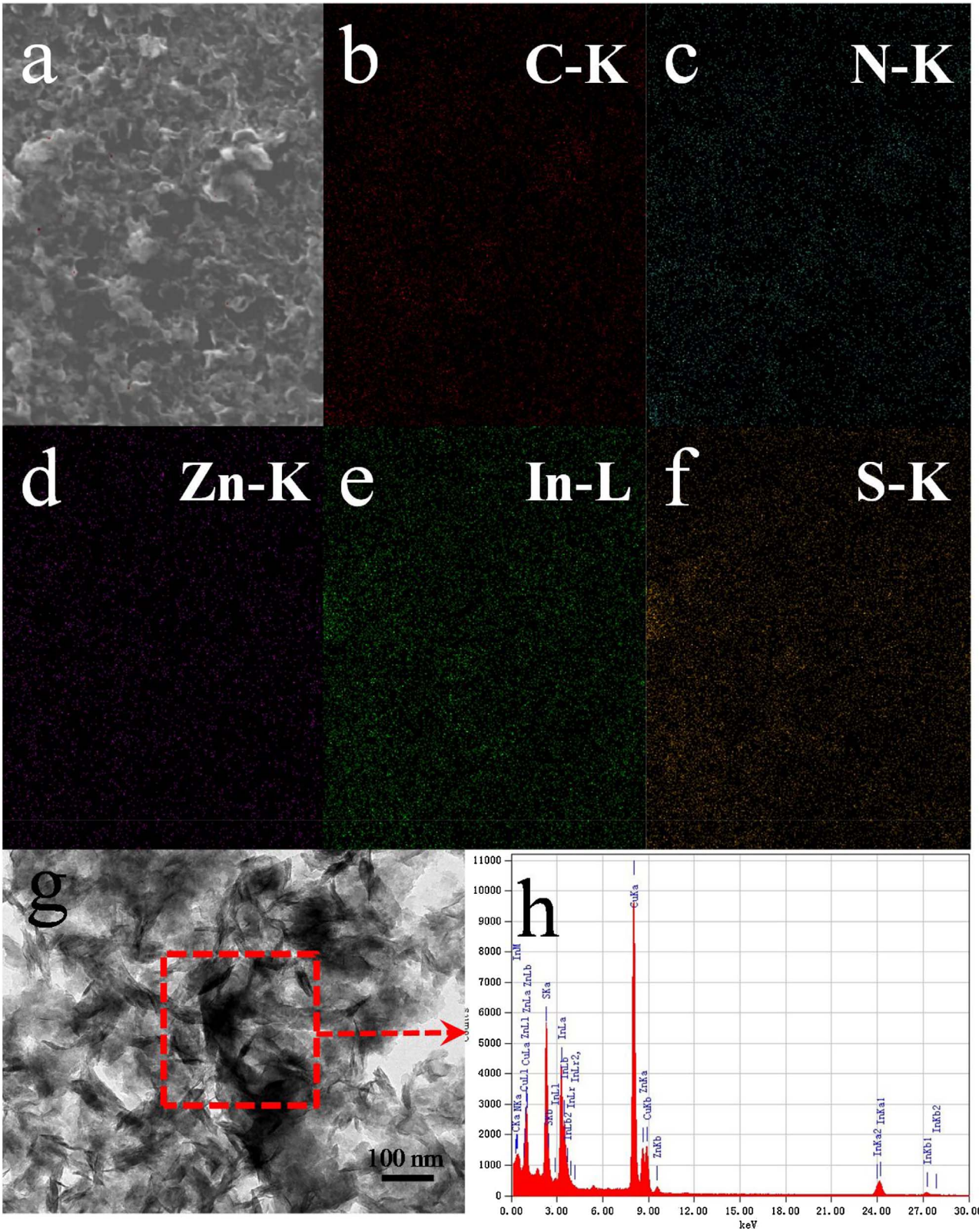

Fig. 5. Elemental mapping of (a) GN@ZN with the spatially resolved elements of (b) carbon, (c) nitrogen, (d) zinc, (e) indium and (f) sulfur. EDX images (g, h) of GN@ZN. The strong peaks for Cu are derived from the carbon-supported copper net applied to load the samples in TEM test.

Therefore, it is advisable and reasonable to investigate the intrinsic link between the three scientific issues and the catalytic performance of H_2 generation for 2D/2D GN@ZN.

Firstly, the sunlight absorption capacity for the preparative samples has been studied by UV–vis diffuse reflectance spectra (DRS). As shown in Fig. 8a, the BCN shows a steep photoabsorption edge at 461 nm, corresponding to an estimated band gap of 2.69 eV, indicating the marginal visible-light absorption. After thermal exfoliation treatment, the resultant g-C_3N_4 nanosheet displays slight hypsochromic shift from 461 nm to 456 nm (relevant band gap of 2.72 eV), this phenomenon is

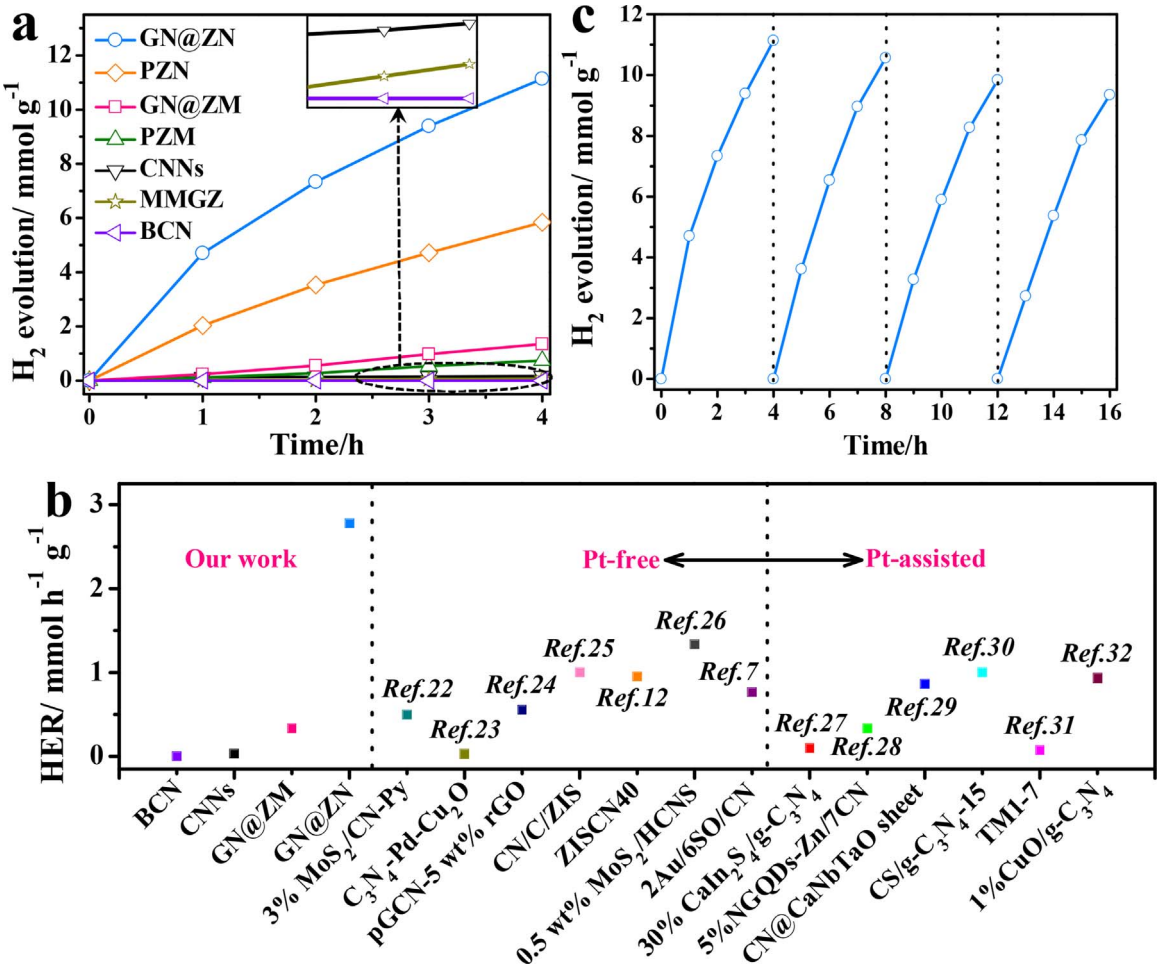

Fig. 6. (a) Time-dependent photocatalytic hydrogen evolution over different photocatalysts without the additive Pt cocatalyst under visible-light irradiation (λ ≥ 420 nm). (b) Hydrogen-evolution rate (HER) over different photocatalysts in this work by contrast with the reported work related to the modification of pristine g-C_3N_4 under visible-light irradiation. (c) Cyclic stability study of photocatalytic hydrogen evolution over GN@ZN without the additive Pt cocatalyst under visible-light irradiation (λ ≥ 420 nm).

due to the quantum confinement effect caused by the closely stack and interaction of g-C_3N_4 layers during the thermal treatment process [33,34]. In regard to the samples of $ZnIn_2S_4$ microsphere and $ZnIn_2S_4$ nanoleaf, the broad visible-light absorption regions at up to 620 nm and 622 nm (relevant band gaps of 2.0 eV and 1.99 eV, respectively) can be clearly found in the corresponding UV–vis DRS profiles of PZM and PZN, respectively, suggestive of a strong optical absorption ability of $ZnIn_2S_4$ material [12,35]. It is noted that PZN shows the much higher intensity in the range of 515–800 nm than PZM, this is because the nano-sized leafy $ZnIn_2S_4$ has more contact areas with the visible light. By contrast with BCN and CNNs, obvious red shifts appear in the absorption edges of 2D/2D GN@ZN and 2D/0D GN@ZM, and their visible-light harvesting abilities are greatly enhanced, indicating that the construction of g-C_3N_4@$ZnIn_2S_4$ binary heterojunction composite effectively improves the sunlight absorption capacity of pure g-C_3N_4. However, the visible-light response of 2D/2D GN@ZN is much poorer than that of 2D/0D GN@ZM, which can be attributed to the photosensitization of $ZnIn_2S_4$ because only a little $ZnIn_2S_4$ nanosheets are

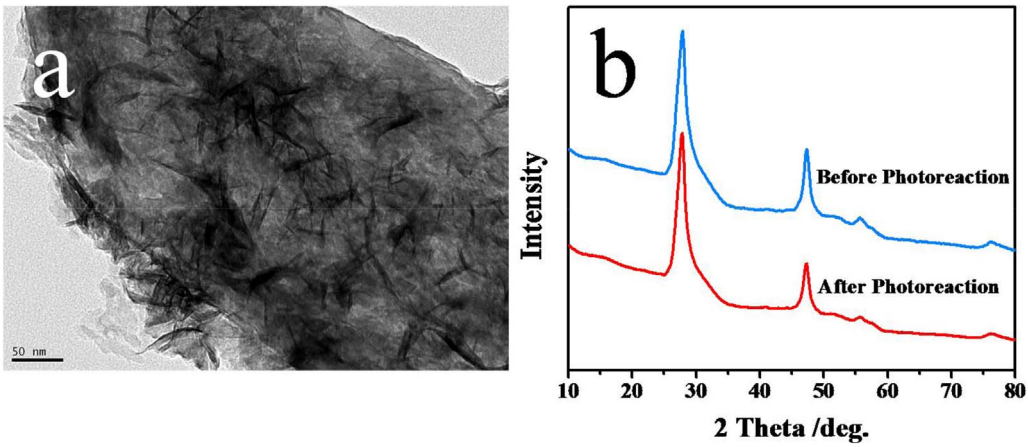

Fig. 7. TEM image (a) of GN@ZN after cyclic stability tests. X-ray diffraction patterns (b) of GN@ZN before and after four photoreactions.

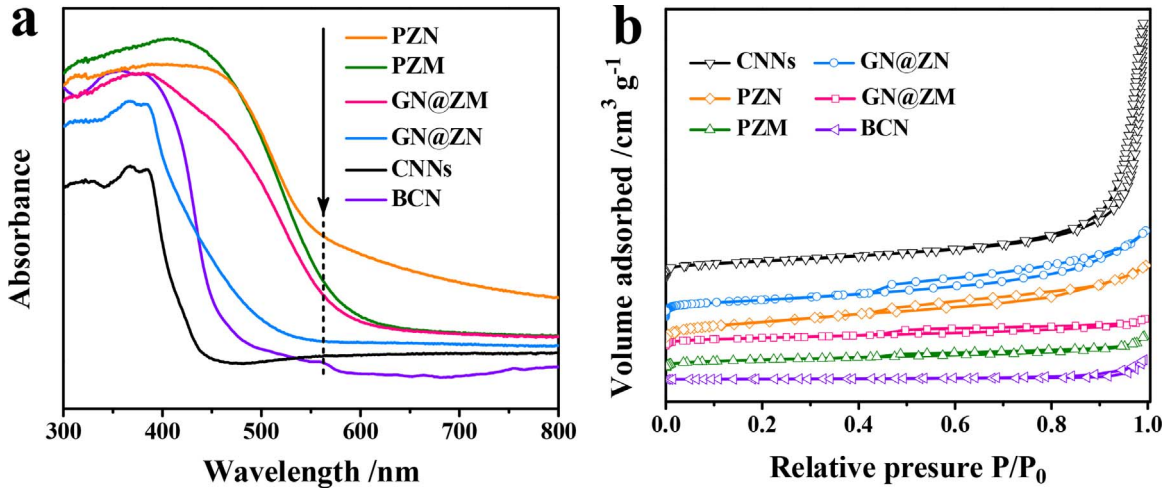

Fig. 8. UV–vis diffuse reflectance spectra (DRS) (a) and nitrogen adsorption-desorption isotherms (b) for BCN, CNNs, PZM, PZN, GN@ZM and GN@ZN.

grown on the surface of CNNs flat in 2D/2D GN@ZN composite.

Secondly, it is of great significance for exploring the changes of textural properties for obtained products. As illustrated in Fig. 8b, all photocatalysts display the typical IV N_2 adsorption-desorption isotherms with a H3-type hysteresis loop, indicative of the presence of mesopores [10,36]. The textural properties of all samples are shown in Table 1. The bulk g-C_3N_4 has low active surface area (11.31 $m^2 g^{-1}$), while the thermal exfoliated g-C_3N_4 sample exhibits significantly enlarged surface area (209.73 $m^2 g^{-1}$). Moreover, compared with the PZM sample (113.67 $m^2 g^{-1}$), the $ZnIn_2S_4$ nanoleaf possesses clearly enhanced active surface area of 152.27 $m^2 g^{-1}$, indicating the structure-induced textural advantages of nanoleafy structure. Accompanied by the construction of binary heterojunction system, both the two g-C_3N_4@$ZnIn_2S_4$ composites (117.42 $m^2 g^{-1}$ and 186.53 $m^2 g^{-1}$ for 2D/0D GN@ZM and 2D/2D GN@ZN, respectively) show the clearly reduced active surface area in comparison with CNNs, this is attributed to the covering of $ZnIn_2S_4$ on the surface of g-C_3N_4 nanosheet to block a large number of mesopore existed in the CNNs.

Furthermore, the photoinduced charge separation and migration efficiencies of the as-prepared photocatalysts have been investigated by photoluminescence (PL) spectra, transient photocurrent responses and electrochemical impedance spectroscopy. As displayed in Fig. 9a, an extremely intense and broad emission peak at 461 nm can be easily observed in the PL spectrum of BCN, suggestive of a fairly high photoinduced charge recombination rate due to the intrinsic geometry structure of bulk g-C_3N_4 [7]. A slight blue-shift can be found in curve of CNNs because of its widening band gap, and its fluorescence is slightly quenched, indicating a suppression of photoinduced charge recombination to a certain extent. Astonishingly, the fluorescence of two g-C_3N_4@$ZnIn_2S_4$ composite samples has been dramatically quenched, indicative of the advantages of binary heterojunction on the separation and migration of photoinduced charges. Notably, 2D/2D GN@ZN displays the far lower emission peak intensity than 2D/0D GN@ZM, demonstrating that the creation of 2D/2D heterojunction with high-speed charge transfer nanochannels greatly accelerates the charge separation and transfer. By contrast with the g-C_3N_4 series samples, the two pure $ZnIn_2S_4$ samples show the extremely low fluorescence intensity due to the intrinsic properties of $ZnIn_2S_4$ material (Fig. 9b), and the PZN exhibits much lower fluorescence intensity than PZM, suggesting that the successful construction of $ZnIn_2S_4$ nanoleaves can effectively promote the photogenerated charge separation and migration in the photoreaction [8,37]. These above results can be further evidenced by transient photocurrent response measurements and electrochemical impedance spectroscopy (EIS). As shown in Fig. 9c, the 2D/2D GN@ZN sample shows an extremely high photocurrent response than BCN, CNNs, PZM, PZN and 2D/0D GN@ZM, and also has the smallest radius of Nyquist circle in Fig. 9d, both suggesting that the 2D/2D GN@ZN sample possesses the dramatically decreased charge transfer resistance and excellent charge separation efficiency [38,39].

To further shed light on the effects of 2D/2D heterojunction with high-speed charge transfer nanochannels on the photoinduced charge separation and transfer efficiency, the transient fluorescence decay spectra for 2D/0D GN@ZM and 2D/2D GN@ZN have been tested. As shown in Fig. 9e, the fluorescent intensities for 2D/0D GN@ZM and 2D/2D GN@ZN display double-exponential decay kinetics. The fitting kinetic parameters (including two radiative lifetimes and their relative amplitudes) of the two g-C_3N_4@$ZnIn_2S_4$ composite samples are summarized in Table 2. The short lifetime (τ_1) of charge carriers increases from 2.29 ns (2D/0D GN@ZM) to 2.82 ns (2D/2D GN@ZN), and the long lifetime (τ_2) for charge carriers clearly increases from 11.97 ns (2D/0D GN@ZM) to 17.95 ns (2D/2D GN@ZN), these results manifest that massive $ZnIn_2S_4$ nanoleaves uniformly distribute on the surfaces of g-C_3N_4 nanosheet flat, thus generates vast contact interfaces and plentiful high-speed charge transfer nanochannels, contributing to a high-efficiency charge separation and transfer as well as a significantly prolonged radiative lifetime of charge carriers [40,41].

As a function of the above studies of three key scientific issues, it is wise to systematically reveal the main factors for remarkable photocatalytic activity. To begin with, it is interesting to compare and analyze the basis data of PZM and 2D/0D GN@ZM samples. As above mentioned, PZM and 2D/0D GN@ZM have the extremely close active surface areas (113.67 $m^2 g^{-1}$ and 117.42 $m^2 g^{-1}$ for PZM and 2D/0D GN@ZM, respectively, Table 1). And PZM and 2D/0D GN@ZM also exhibit quite close transient photocurrent response (Fig. 9c) and EIS Nyquist radius (Fig. 9d), indicative of the close photoinduced charge separation and migration efficiency. Only the visible-light absorption capacity of PZM is much stronger than that of 2D/0D GN@ZM (DRS analysis in Fig. 8a). These aforementioned data mean that if the sunlight absorption capacity plays a vital role in the photocatalytic hydrogen evolution activity, PZM would display much higher

Table 1
Textural properties for BCN, CNNs, PZM, PZN, GN@ZM and GN@ZN.

Samples	S_{BET} ($m^2 g^{-1}$)	Average pore size (nm)	Pore volume ($cm^3 g^{-1}$)
BCN	11.31	37.52	0.10
CNNs	209.73	25.36	1.27
PZM	113.67	5.81	0.17
PZN	152.27	4.07	0.28
GN@ZM	117.42	6.27	0.17
GN@ZN	186.53	7.19	0.38

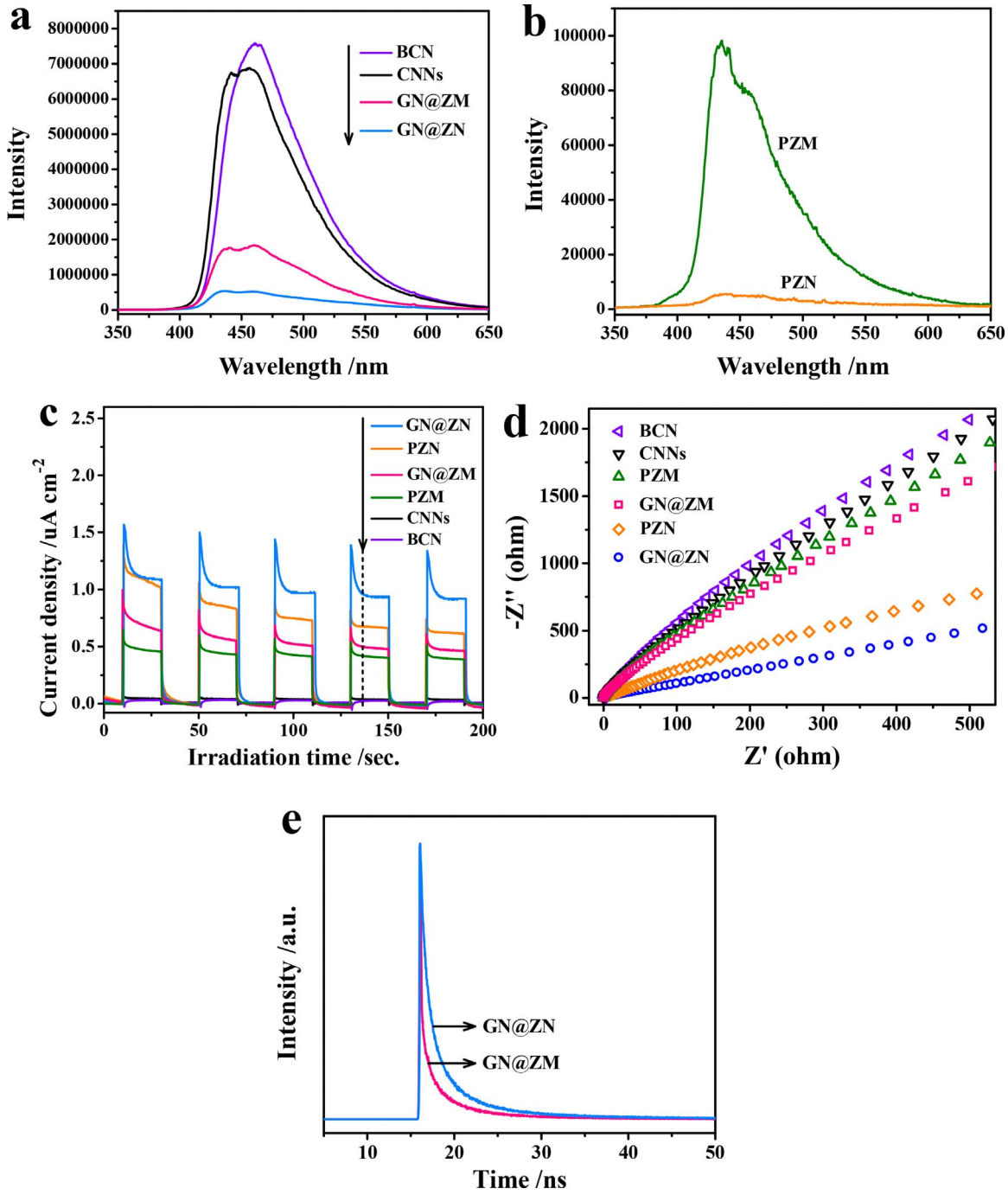

Fig. 9. (a) Photoluminescence (PL) spectra of BCN, CNNs, GN@ZM and GN@ZN. (b) Photoluminescence spectra (PL) of PZM and PZN. (c) Transient photocurrent responses and (d) EIS Nyquist plots of BCN, CNNs, PZM, PZN, GN@ZM and GN@ZN. (e) Transient fluorescence decay spectra for GN@ZM and GN@ZN.

Table 2
The fitted fluorescence lifetimes and corresponding amplitudes of photoinduced charge carriers in GN@ZM and GN@ZN.

Samples	τ_1 (ns) (Rel.%)	τ_2 (ns) (Rel.%)
GN@ZM	2.29 (42.29)	11.97 (57.71)
GN@ZN	2.82 (39.85)	17.95 (60.15)

photocatalytic activity in comparison with 2D/0D GN@ZM. However, PZM (0.18 mmol h^{-1} g^{-1}) shows a far lower photocatalytic activity relative to 2D/0D GN@ZM (0.34 mmol h^{-1} g^{-1}). All above results show that the optical absorption capacity maybe not the key factor to promote the enhancement of photocatalytic activity of the g-C_3N_4/$ZnIn_2S_4$ composite samples.

As the above analysis, the influences of optical absorption capacity on the HER performance for CNNs and BCN could be neglected. Besides, it is clearly found that the CNNs and BCN samples have the very close PL intensity (Fig. 9a), transient photocurrent response (Fig. 9c) and EIS Nyquist radius (Fig. 9d), suggesting the close charge separation and migration efficiency. Furthermore, CNNs exhibits much larger active surface area (209.73 m^2 g^{-1}) by contrast with BCN (11.31 m^2 g^{-1}). However, CNNs does not show a greatly enhanced HER value compared with BCN as expected (Fig. 6a). These results demonstrate that the larger active surface area could hardly contribute to the higher photocatalytic H_2 evolution activity for the obtained products. This

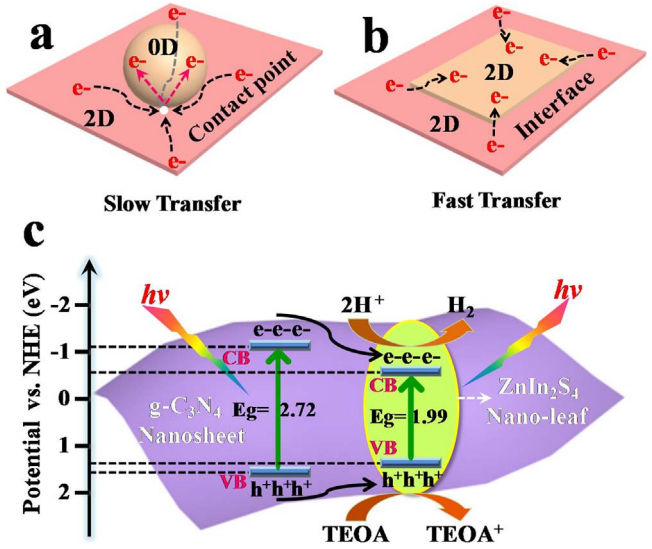

Fig. 10. Schematic illustration of contact interfaces for (a) 2D/0D heterojunction and (b) 2D/2D heterojunction. (c) Proposed mechanism of charge transfer for photocatalytic hydrogen evolution over GN@ZN under visible light irradiation (λ ≥ 420 nm).

conclusion is evidenced immediately by the heterojunction construction for 2D/0D GN@ZM. The introduction of $ZnIn_2S_4$ microspheres on the CNNs flat significantly reduces the active surface area in comparison with original CNNs (117.42 $m^2\ g^{-1}$ and 209.73 $m^2\ g^{-1}$ for 2D/0D GN@ZM and CNNs, respectively), however, the HER value of 2D/0D GN@ZM (0.34 mmol $h^{-1}\ g^{-1}$) has indeed improved a lot than that of CNNs (0.04 mmol $h^{-1}\ g^{-1}$). These above basic data comparisons reveal that the active surface area is also not the main factor for the enhanced photocatalytic HER activity of the g-C_3N_4/$ZnIn_2S_4$ composite samples.

Up to this point, only the last factor is left to discuss, that is whether the photoinduced charge separation and migration efficiency is the key factor for the enhancement of photocatalytic HER activity or not. This question can be solved by the analysis of HER activity between 2D/0D GN@ZM and 2D/2D GN@ZN, as well as between 2D/2D GN@ZN and MMGZ. According to the steady PL spectra (Fig. 9a), transient photocurrent response (Fig. 9c), EIS Nyquist radius (Fig. 9d) and transient fluorescence decay spectra (Fig. 9e), when micron-sized $ZnIn_2S_4$ microspheres have grown on the surfaces of g-C_3N_4 nanosheet flat in the face-to-point way, and only a small quantity of charge transfer nanochannels can be generated in the 2D/0D GN@ZM sample (Fig. 10a), resulting in a slow charge transport efficiency and limited photocatalytic HER activity. However, the uniformly distributed $ZnIn_2S_4$ nanoleaves on g-C_3N_4 nanosheet flat with face-to-face contact way can construct plentiful high-speed charge transfer nanochannels (Fig. 10b), which strongly accelerate the high-efficiency separation and migration for the photogenerated charges, ultimately contributing to a remarkable HER (2.78 mmol $h^{-1}\ g^{-1}$) and a high AQY (7.05%). The importance of the above 2D/2D heterojunction with high-speed charge transfer nanochannels is also well evidenced through the comparison with a mechanically mixed g-C_3N_4 nanosheet and $ZnIn_2S_4$ nanoleaf sample (MMGZ). Due to a lack of high-speed charge transfer nanochannels, the photoinduced charges are severely recombined in MMGZ, leading to the negligible HER (0.02 mmol $h^{-1}\ g^{-1}$). Based on the above analysis, it is confidently concluded that the outstanding photocatalytic H_2 evolution activity of 2D/2D g-C_3N_4 nanosheet@$ZnIn_2S_4$ nanoleaf is mainly derived from the high photoinduced charge separation and migration efficiency by the formation of well-designed high-speed charge transfer nanochannels.

According to the aforementioned results and discussion, a proposed mechanism of charge transfer for photocatalytic hydrogen evolution has been put forward in the presence of the 2D/2D g-C_3N_4 nanosheet@$ZnIn_2S_4$ nanoleaf photocatalyst under visible light irradiation

Table 3
The estimated values of band gap energy, valence band potential and conduction band potentials over g-C_3N_4 nanosheet (CNNs) and $ZnIn_2S_4$ nanoleaf (PZN).

Samples	Band gap energy (eV)	Valence band potential (eV)	Conduction band potential (eV)
CNNs	2.72	1.59	−1.13
PZN	1.99	1.36	−0.63

(λ ≥ 420 nm). As illustrated in Fig. 10c, due to the appropriate conduction band (CB) and valence band (VB) positions for g-C_3N_4 nanosheet and $ZnIn_2S_4$ nanoleaf (Table 3), the type-I binary heterojunction interfaces were formed, thus providing the prerequisite for the generation of the 2D/2D heterojunction with high-speed charge transfer nanochannels. When g-C_3N_4 nanosheet and $ZnIn_2S_4$ nanoleaf were illuminated by the visible light, both of them could be excited to produce massive photogenerated electron-hole pairs [42]. Due to the huge CB potential difference between the CB of g-C_3N_4 nanosheet and $ZnIn_2S_4$ nanoleaf (Table 3), the photoinduced electrons on the CB of g-C_3N_4 nanosheet could readily transfer to the CB of $ZnIn_2S_4$ nanoleaf via the 2D/2D heterojunction interfaces at a fast charge transport rate (Fig. 10b) [43], then reduce the hydrogen ions in aqueous solution to generate hydrogen. While the photogenerated holes on the VB of g-C_3N_4 nanosheet transferred to the VB of $ZnIn_2S_4$ nanoleaf, then these holes were quickly quenched by the sacrificial electron donor of TEOA. It should be emphasized that the synergistic effect of 2D g-C_3N_4 nanosheet, 2D $ZnIn_2S_4$ nanoleaf and 2D/2D heterojunction interfaces contributes to the formation of unique high-speed charge transfer nanochannels in the heterojunction system. These high-speed charge transfer nanochannels endowed by the 2D/2D heterojunction greatly shorten the charge migration distance and transfer time, significantly enhance the charge transport and separation efficiency, ultimately leading to a remarkable HER activity without the additive Pt cocatalyst for the 2D/2D g-C_3N_4 nanosheet@$ZnIn_2S_4$ nanoleaf.

4. Conclusions

In summary, a novel 2D/2D g-C_3N_4 nanosheet@$ZnIn_2S_4$ nanoleaf has been well designed and prepared via in-situ growing unique $ZnIn_2S_4$ nanoleaves on the surfaces of g-C_3N_4 nanosheets in the face-to-face way. The unusual 2D/2D heterojunction geometry significantly enlarges the contact areas relative to 2D/0D face-to-point one (g-C_3N_4 nanosheet@$ZnIn_2S_4$ microsphere sample). More importantly, the 2D/2D heterojunction can produce the plentiful high-speed charge transfer nanochannels in g-C_3N_4 nanosheet@$ZnIn_2S_4$ nanoleaf composite, which mean that the photogenerated charges could migrate along the g-C_3N_4 nanosheet to the 2D/2D heterojunction interface then to $ZnIn_2S_4$ nanoleaf, this process contributes to a fairly high photoinduced charge separation and migration efficiency, ultimately resulting in a remarkable visible-light-driven HER activity without the additive Pt cocatalyst, nearly 69.5, 15.4, 8.2 and 1.9 times higher than that of pure g-C_3N_4 nanosheet, pure $ZnIn_2S_4$ microsphere, 2D/0D g-C_3N_4 nanosheet@$ZnIn_2S_4$ microsphere and pure $ZnIn_2S_4$ nanoleaf, respectively. This work offers a new insight for the design and preparation of binary heterojunction composite with highly-efficient charge separation and transfer.

Acknowledgements

All authors acknowledge the financial support from the National Natural Science Foundation of China (Grant No. 21303130), the Natural Science Basic Research Plan in Shaanxi Province of China (Grant No. 2017JZ001), the State Key Laboratory of Heavy Oil Processing (Grant No. SKLOP201602001) and the Fundamental Research Funds for the Central Universities. The authors are also

grateful for the technical help from International Center for Dielectric Research (ICDR), Xi'an Jiaotong University, Xi'an, China. Thanks to Mr. Ma and Ms. Dai for the help of using TEM, SEM and EDX.

References

[1] J. Wang, Y. Chen, Y. Shen, S. Liu, Y. Zhang, Chem. Commun. 53 (2017) 2978–2981.
[2] A. Lin, D. Qi, H. Ding, L. Wang, M. Xing, B. Shen, J. Zhang, Catal. Today 281 (2017) 636–641.
[3] Q. Zhang, Y. Huang, S. Peng, Y. Zhang, Z. Shen, J. Cao, W. Ho, S.C. Lee, D.Y.H. Pui, Appl. Catal. B: Environ. 204 (2017) 346–357.
[4] B. Lin, G. Yang, B. Yang, Y. Zhao, Appl. Catal. B: Environ. 198 (2016) 276–285.
[5] J.C. Theriot, C.H. Lim, H. Yang, M.D. Ryan, C.B. Musgrave, G.M. Miyake, Science 352 (2016) 1082–1086.
[6] D.M. Schultz, T.P. Yoon, Science 343 (2014) 1239176.
[7] A. Zada, M. Humayun, F. Raziq, X. Zhang, Y. Qu, L. Bai, C. Qin, L. Jing, H. Fu, Adv. Energy Mater. 6 (2016) 1601190.
[8] R. Wang, L. Gu, J. Zhou, X. Liu, F. Teng, C. Li, Y. Shen, Y. Yuan, Adv. Mater. Interfaces 2 (2015) 1500037.
[9] Z. Tong, D. Yang, Y. Sun, Y. Nan, Z. Jiang, Small 12 (2016) 4093–4101.
[10] W. Chen, T. Liu, T. Huang, X. Liu, X. Yang, Nanoscale 8 (2016) 3711–3719.
[11] W. Chen, Y. Hua, Y. Wang, T. Huang, T. Liu, X. Liu, J. Catal. 349 (2017) 8–18.
[12] H. Liu, Z. Jin, Z. Xu, Z. Zhang, D. Ao, RSC Adv. 5 (2015) 97951–97961.
[13] N.S. Chaudhari, S.S. Warule, B.B. Kale, RSC Adv. 4 (2014) 12182–12187.
[14] K. Song, R. Zhu, F. Tian, G. Cao, F. Ouyang, J. Solid State Chem. 232 (2015) 138–143.
[15] W. Chen, T. Liu, T. Huang, X. Liu, J. Zhu, G. Duan, X. Yang, J. Mater. Sci. 50 (2015) 8142–8152.
[16] W.J. Ong, L.L. Tan, S.P. Chai, S.T. Yong, A.R. Mohamed, Nano Energy 13 (2015) 757–770.
[17] Z. Zhang, J. Huang, M. Zhang, Q. Yuan, B. Dong, Appl. Catal. B: Environ. 163 (2015) 298–305.
[18] C. Han, Y. Wang, Y. Lei, B. Wang, N. Wu, Q. Shi, Q. Li, Nano Res. 8 (2015) 1199–1209.
[19] M.J.M. Batista, O.F. Carceller, A. Kubacka, M.F. García, Appl. Catal. B: Environ. 203 (2017) 663–672.
[20] N.S. Chaudhari, A.P. Bhirud, R.S. Sonawane, L.K. Nikam, S.S. Warule, V.H. Rane, B.B. Kale, Green Chem. 13 (2011) 2500–2506.
[21] L. Mandal, N.S. Chaudhari, S. Ogale, ACS Appl. Mater. Interfaces 5 (2013) 9141–9147.
[22] M. Li, L. Zhang, X. Fan, M. Wu, Y. Du, M. Wang, Q. Kong, L. Zhang, J. Shi, Appl. Catal. B: Environ. 190 (2016) 36–43.
[23] W. Yin, L. Bai, Y. Zhu, S. Zhong, L. Zhao, Z. Li, S. Bai, ACS Appl. Mater. Interfaces 8 (2016) 23133–23142.
[24] C. Pu, J. Wan, E. Liu, Y. Yin, J. Li, Y. Ma, J. Fan, X. Hu, Appl. Surf. Sci. 399 (2017) 139–150.
[25] F. Shi, L. Chen, M. Chen, D. Jiang, Chem. Commun. 51 (2015) 17144–17147.
[26] D. Zheng, G. Zhang, Y. Hou, X. Wang, Appl. Catal. A: Gen. 521 (2016) 2–8.
[27] D. Jiang, J. Li, C. Xing, Z. Zhang, S. Meng, M. Chen, ACS Appl. Mater. Interfaces 7 (2015) 19234–19242.
[28] M. Yan, Y. Hua, F. Zhu, L. Sun, W. Gu, W. Shi, Appl. Catal. B: Environ. 206 (2017) 531–537.
[29] S. Thaweesak, M. Lyu, P. Peerakiatkhajohn, T. Butburee, B. Luo, H. Chen, L. Wang, Appl. Catal. B: Environ. 202 (2017) 184–190.
[30] K. Li, X. Xie, W. Zhang, Carbon 110 (2016) 356–366.
[31] S. Shen, D. Zhao, J. Chen, L. Guo, S.S. Mao, Appl. Catal. A: Gen. 521 (2016) 111–117.
[32] B. Li, Y. Wang, Y. Zeng, R. Wang, Mater. Lett. 178 (2016) 308–311.
[33] Q. Han, B. Wang, J. Gao, Z. Cheng, Y. Zhao, Z. Zhang, L. Qu, ACS Nano 10 (2016) 2745–2751.
[34] H. Xu, J. Yan, X. She, L. Xu, J. Xia, Y. Xu, Y. Song, L. Huang, H. Li, Nanoscale 6 (2014) 1406–1415.
[35] L. Bo, K. He, N. Tan, B. Gao, Q. Feng, J. Liu, L. Wang, J. Environ. Manage. 190 (2017) 259–265.
[36] B. Lin, H. An, X. Yan, T. Zhang, J. Wei, G. Yang, Appl. Catal. B: Environ. 210 (2017) 173–183.
[37] Z. Yan, Z. Sun, X. Liu, H. Jia, P. Du, Nanoscale 8 (2016) 4748–4756.
[38] K. Saravanakumar, R. Karthik, S. Chen, J.V. Kumar, K. Prakash, V. Muthuraj, J. Colloid Interface Sci. 504 (2017) 514–526.
[39] S.B. Kokane, R. Sasikala, D.M. Phase, S.D. Sartale, J. Mater. Sci. 52 (2017) 7077–7090.
[40] Y.C. Pu, H.Y. Chou, W.S. Kuo, K.H. Wei, Y.J. Hsu, Appl. Catal. B: Environ. 204 (2017) 21–32.
[41] F. He, G. Chen, Y. Zhou, Y. Yu, L. Li, S. Hao, B. Liu, J. Mater. Chem. A 4 (2016) 3822–3827.
[42] B. Lin, S. Chen, F. Dong, G. Yang, Nanoscale 9 (2017) 5273–5279.
[43] C. Xue, T. Zhang, S. Ding, J. Wei, G. Yang, ACS Appl. Mater. Interfaces 9 (2017) 16091–16102.